Communication

D-A-D structured selenadiazolesbenzothiadiazole-based near-infrared dye for enhanced photoacoustic imaging and photothermal cancer therapy

Zijin Cheng[a], Tian Zhang[a], Weili Wang[a], Qing Shen[a], Ying Hong[a], Jinjun Shao[a,*], Xiaoji Xie[a], Zhenghao Fei[b,*], Xiaochen Dong[a,c]

[a] Key Laboratory of Flexible Electronics (KLOFE) and Institute of Advanced Materials (IAM), Nanjing Tech University, Nanjing 210009, China
[b] Applied Chemistry & Environmental Engineering, Yancheng Teachers University, Yancheng 224051, China
[c] School of Chemistry and Materials Science, Nanjing University of Information Science & Technology, Nanjing 210044, China

ABSTRACT

Near-infrared (NIR) small molecular organic dyes as photothermal agents for cancer photothermal therapy (PTT) have attracted considerable research attention. Herein, two donor-acceptor-donor (D-A-D) structured NIR dyes, BBTT and SeBTT, are rationally designed, where the only difference is one heteroatom within the acceptor unit varying from sulfur to selenium (Se). More importantly, SeBTT NPs exhibit stronger NIR absorbance and higher photothermal conversion efficiency (PTCE $\approx$ 65.3%). *In vivo* experiments illustrate that SeBTT NPs can be utilized as a high contrast photoacoustic imaging (PAI) agent, and succeed in tumor suppression without noticeable damage to main organs under NIR photoirradiation. This study presents an effective molecular heteroatom surgery strategy to regulate the photothermal properties of NIR small molecules for enhanced PAI and PTT.

© 2021 Chinese Chemical Society and Institute of Materia Medica, Chinese Academy of Medical Sciences. Published by Elsevier B.V. All rights reserved.

Photothermal therapy (PTT) is an emerging effective cancer treatment for various tumorous diseases; it has recently attracted ever-increasing research attention due to its inherent advantages of high tumor eradication efficacy, low side effects as well as the auxiliary real-time diagnosis function for the theranostic platform [1–3]. In PTT, photothermal materials should convert the absorbed photons to thermal energy to induce local hyperthermia for tumor ablation. To achieve high therapeutic performance, near-infrared (NIR) photothermal agents are highly desired owing to minimized photon scattering and diminished tissue auto-fluorescence, thus achieving deeper tissue penetration depth and less photo-damage to the living human body. Accordingly, it is significant to exploit novel NIR photothermal agents for cancer phototheranostics [4–8].

Besides, PTT associated with photoacoustic imaging (PAI) has gained extensive attention by virtue of the intrinsic benefits [9,10]. The integration of diagnosis and phototherapy in a single nanoplatform not only can improve the therapeutic efficiency but also accurately probe tumor location. Moreover, the NIR contrast agent for PAI can achieve a high signal-to-noise ratio on account of the low signal attenuation. Both PAI and PTT are highly dependent on the photothermal conversion performance of the agents; as a result, considerable research attention has been focused on the development of NIR nanotheranostic agents with high photothermal conversion efficiency for PAI-guided PTT for cancer treatment [11–16].

To date, photothermal materials mainly include inorganic nanomaterials [17–19] and organic nanomaterials [20–23]. In spite of the wide employment of inorganic materials for PTT, these nanomaterials bear the inherent shortcomings of poor biosafety. Hence, it prompts us to expand the library of organic dyes for PTT, such as indocyanine green (ICG) with superior biocompatibility. As a matter of fact, ICG has been approved as a clinical contrast agent by the USA Food and Drug Administration (FDA), and it has already been intensively studied as an off-label phototherapeutic agent [24,25]. Nonetheless, ICG possesses its own limitations of photobleachability and poor photothermal behavior, as needs to be addressed before it is widely employed in PTT. Therefore, many small molecular organic NIR dyes have been rationally developed as photothermal agents to replace ICG [26,27]. Although different types of organic NIR dyes as photothermal agents based on diketopyrrolopyrrole (DPP) [28–31],

Boron dipyrromethane (BODIPY) [32–36] or benzo[c][1,2,5]-thiadiazole [37,38], have emerged and achieved remarkable progress in recent years, it is still an urgent demand to continue to pursue origin small molecular organic NIR dyes with the merits of fine structure/property tuning, well-defined chemical structures, and good repeatability, that have high photothermal conversion efficiency and high stability [39–42].

Selenium (Se), coming from the VIA group, is a semi-metallic element. Besides, it is an essential element in the organism which fulfills many significant biochemical functions. Se-containing molecules can facilitate the immune-cell activity to impede tumor growth by regulating the reactive oxygen species (ROS) level to balance the redox equilibrium in the human body [43,44]. And a family of Se-containing small molecules has been developed as the redox trigger for smart drug delivery systems [45–47]. Besides, owing to the special electronegativity and atomic radius of Se, Se-containing π-conjugated systems demonstrate narrow energy gaps and unique chemical photophysical behaviors. Benzobisthiadiazole (BBT), a 14π-electron system with a hypervalent S atom, is one of the most robust electron-withdrawing building blocks for low bandgap compounds construction since its first report by Yamashita et al. in the 1980s [48–50]. By replacing the S with Se in the BBT heterocycles to get its analog selenadiazolesbenzothiadiazole (SeBT), a narrower energy gap and pronounced red-shift can be observed, because electrons of Se in the valence band can be populated to the conduction band under photoirradiation [51–53]. To achieve a bathochromic shift of SeBT derivative and push the absorption band more redshifted, the donor (D)-acceptor (A) structural design strategy is commonly employed for the NIR molecule construction [54–57].

Herein, two small molecular organic NIR dyes BBTT and SeBTT with D-A-D scaffold, were rationally developed as photothermal agents for PTT (Scheme 1). The chemical structures of the two NIR dyes are the same except for one heteroatom difference of S and Se. Through nano-precipitation, hydrophilic NPs were obtained. The absorption of both NPs showed pronounced red-shift, and SeBTT NPs showed a higher photothermal conversion efficacy of 65.3% than BBTT NPs of 55.1%, which is probably due to the polar effect of the heavier atom Se. Moreover, SeBTT NPs can efficiently kill HeLa cells with a half-maximal inhibitory concentration of as low as 20 μg/mL. In vivo studies demonstrate that upon 808 nm NIR photoirradiation, SeBTT NPs can accomplish PAI-guided PTT, without noticeable side effect on the major organs.

As shown in Fig. 1a, compound 1 was synthesized according to the previous report [58]. Intermediate 2 was synthesized by nitration of 1 with an acid mixture of fuming HNO_3 and CF_3SO_3H, followed by Stille coupling with 3 to afford 4 in 75% yield [23]. The n-hexyl hydrocarbon chain attached to the thiophene ring was introduced to improve the solubility and processability. Later, 4 was reduced by iron dust in acetic acid to give the air-stable diamine 5 [59]. Later, 5 was directly employed for annulation with

selenium dioxide (SeO_2) in THF to produce SeBTT with a moderate yield of 69% [60]. BBTT was successfully prepared by treating 5 with N-thionylaniline (PhNSO) and trimethylchlorosilane (TMSCl) in pyridine for annulation at 80 °C in 68% yield [61]. The two flanked thiophene units were incorporated as an electron donor (D) onto the electron acceptor (A) core to generate the D-A-D scaffold in both SeBTT and BBTT to facilitate intramolecular charge transfer (ICT), thus resulting in a pronounced bathochromic shift [62,63]. The chemical structures of SeBTT and BBTT were verified by ^{1}H NMR, ^{13}C NMR and MALDI-TOF mass spectroscopy (Supporting information). Besides, the frontier molecular orbital profiles of SeBTT and BBTT were simulated by time-dependent density functional theory (TD-DFT at B3LYP/6-31G**) calculations (Fig. S1 in Supporting information). The calculated HOMO/LUMO energy levels were −5.01/−3.47 eV and −4.99/−3.52 eV for SeBTT and BBTT, respectively; Thus, the bandgap is 1.39 eV for SeBTT, and 1.53 eV for BBTT. Additionally, both HOMOs and LUMOs are spread over the molecular backbones, which is beneficial for efficient ICT [2].

The absorbance and photoluminescence (PL) spectra of SeBTT and BBTT in toluene were measured to explore the heteroatom substitution effect on their photophysical behaviors. As shown in Fig. 1b and Fig. S3 (Supporting information), both dyes showed two prominent absorption bands, the one between 300 nm and 400 nm is ascribed to the electronic transitions of both n-π^* and π-π^* within the π-conjugated system; and the other covering from 550 nm to 1000 nm is attributed to the significant ICT effect from periphery electron-rich thiophene units to the central electron-deficient core. SeBTT presents two absorption peaks at 350 nm and 380 nm, as well as a broad band ranging from 600 nm to 1000 nm peaked at 825 nm (ε = 6780 L mol^{-1} cm^{-1}), and the optical absorption edge (λ_{abs}^{onset}) is estimated to be 948 nm. While BBTT shows a similar absorption profile with peaks at 338 nm, 355 nm, and 730 nm (ε = 6830 L mol^{-1} cm^{-1}), and with λ_{abs}^{onset} at 858 nm, thus, the optical band gap (E_g^{opt}) was determined to be 1.31 eV for SeBTT, and 1.44 eV for BBTT, according to equation E_g^{opt} = 1240/λ (eV). In addition, the pronounced red-shift of 90 nm from BBTT to SeBTT is due to the polar effect of the selenium atom. The maximal photoluminescence peak of SeBTT and BBTT in toluene is respectively located at 925 nm and 850 nm, resulting in a large Stokes shift (ν) of 100 nm and 120 nm, respectively.

Hydrophilic SeBTT NPs and BBTT NPs were fabricated through the simple nano-precipitation method. Both NPs can disperse well in water, and the solutions with high transparency are green-yellow for SeBTT NPs and green color for BBTT NPs. As exhibited in Fig. 1c, the dynamic light scattering (DLS) measurement of SeBTT NPs reveals a hydrodynamic mean diameter of 76 nm, slightly larger than that transmission electron microscopy (TEM) result of 50 nm. Meanwhile, BBTT NPs showed similar diameters. For BBTT NPs, the average hydrodynamic diameter is 70 nm, which is a little larger than the result of TEM (40 nm). In addition, after a few months storage under ambient condition, the solutions still kept high transparency, indicating excellent dispersibility of these NPs.

The absorbance and fluorescence spectra of both NPs appear slightly broader than that in toluene (Fig. 1c, Figs. S3 and S4 in Supporting information). SeBTT NPs display a broad and intensive absorbance in the NIR regime covering 650−1050 nm with the peak at 905 nm and the absorption edge at 1021 nm, exhibiting a red-shift of 80 nm than that in toluene. Meanwhile, BBTT NPs show a maximum absorption peak at 785 nm with the absorption edge at 1021 nm, and a red-shift of 60 nm compared to that in toluene can be observed. It is noteworthy that both SeBTT NPs and BBTT NPs showed very weak fluorescence signals in an aqueous solution than in toluene. This is consistent with the aggregation-caused quenching (ACQ) effect, which can facilitate the non-radiative decay for heat generation and promote photothermal performance.
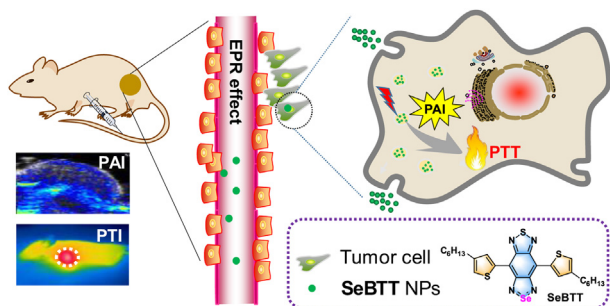
Scheme 1. Schematic illustration of NIR SeBTT NPs for photoacoustic/photothermal imaging-guided PTT.
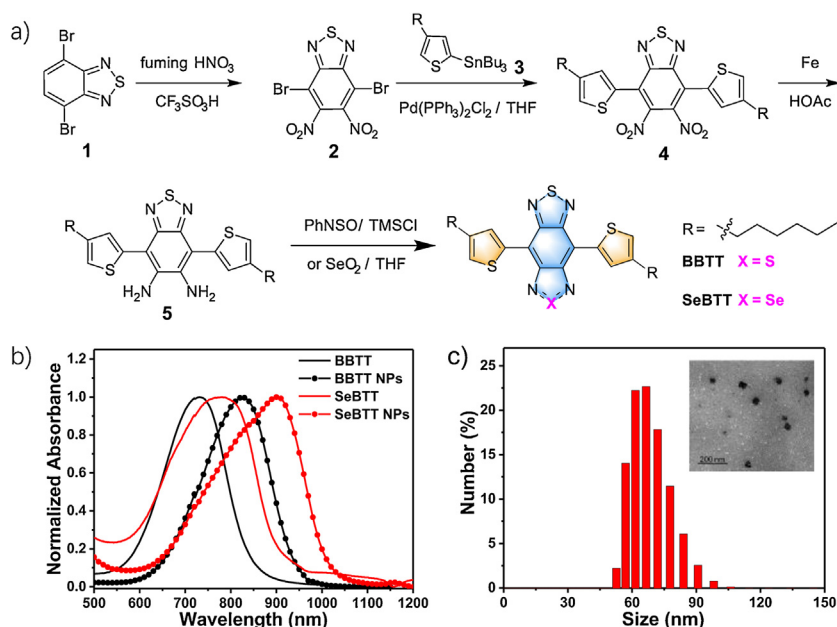
Fig. 1. (a) Synthetic route for SeBTT and BBTT. (b) Normalized UV–vis-NIR absorption spectra for BBTT and SeBTT in toluene and their corresponding NPs in water. (c) DLS size distribution and TEM image (inset) for SeBTT NPs.

The photothermal conversion properties for both SeBTT NPs and BBTT NPs were quantitatively evaluated. The photothermal effect was studied by monitoring the temperature change of SeBTT NPs and BBTT NPs at various concentrations (150, 125, 100, 50, and 25 μg/mL) under 808 nm photoirradiation (1.10 W/cm^2, 10 min) (Fig. 2 and Fig. S5 in Supporting information). As shown in Fig. 2a, with the increase of NPs concentration, the solution temperature gradually rises under photoirradiation, indicating the significant concentration-dependent characteristics of photothermal conversion. When the concentration of SeBTT NPs is 150 μg/mL, the temperature increase reaches up to ~30 °C within 10 min, manifesting the outstanding photothermal activity of SeBTT NPs. In comparison, the aqueous BBTT NPs show a temperature increase of 24 °C under the same condition. While water, taken as a control, just showed a slight temperature change of 2.0 °C only.

Additionally, both SeBTT NPs and BBTT NPs (100 μg/mL) were exposed to 808-nm laser at various power densities (1.10, 0.90, 0.77, 0.44 and 0.10 W/cm^2) for 10 min. The temperature for both NPs elevated along with the rise of the laser power densities, implying the power intensity dependence manner of the photothermal behavior for both NPs (Fig. 2b and Fig. S5). The photothermal conversion efficiency (PTCE) was calculated to be 65.3% and 55.1% for SeBTT NPs and BBTT NPs, respectively. SeBTT NPs showed higher PTCE; this is probably on account of polar effect of Se atom in SeBTT molecule. Also, the high PTCE of both NPs are among the best NIR organic photothermal agents [64–66].

Photostability and photothermal stability are of great importance for PTT *in vivo*. Both NPs in water show excellent photothermal stability. The photothermal stability of both NPs was first evaluated for five alternate photoirradiation ON/OFF cycles; And
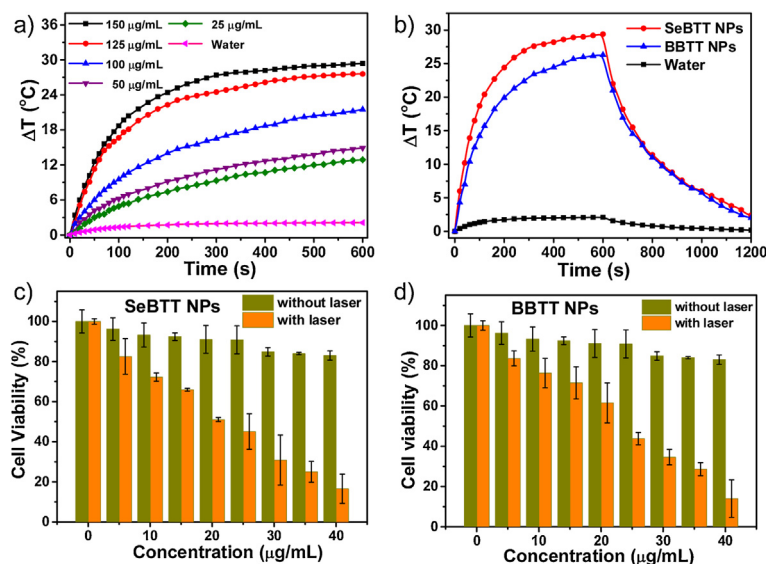

Fig. 2. (a) Temperature change plots of different concentrations of SeBTT NPs upon 808-nm laser irradiation (1.10 W/cm^2, 10 min). (b) Photothermal response of SeBTT NPs and BBTT NPs in water under photoirradiation of 1.10 W/cm^2 at the same concentration (150 μg/mL). Cell viability after treatment with (c) SeBTT NPs and (d) BBTT NPs at various concentrations with/without photoirradiation.

the temperature changes of SeBTT NPs or BBTT NPs presented almost no change (Fig. S6 in Supporting information). Simultaneously, the absorption spectra and apparent colors after five cycles of alternate heating and cooling under irradiation show almost no change. Under Xe lamp irradiation for 2 h, a decomposition of less than 5% can be observed for both NPs, while around 70% of Fluorescein spoiled under the same circumstances for only 60 min (Fig. S7 in Supporting information). Besides, there was no precipitation or aggregates observed after photoirradiation for both NPs, suggesting their outstanding photostability. These results provide solid confirmation that SeBTT NPs and BBTT NPs are equipped with excellent photothermal stability and photostability.

To explore the *in vitro* photothermal effect, 3-(4,5-dimethylthiazol-2-yl)-2,5-diphenyl-tetrazolium bromide (MTT) assay was carried out to study the cytotoxic effect and biocompatibility for both NPs on HeLa cell lines. Two groups of HeLa cells were incubated with SeBTT NPs or BBTT NPs at various concentrations (0, 5, 10, 15, 20, 25, 30, 35, and 40 μg/mL) for 24 h, and then subjected for laser irradiation. The other two groups, incubated SeBTT NPs or BBTT NPs, were kept from irradiation. As presented in Fig. 2, the cell viability under 808 nm laser irradiation is presented to follow a dose-dependent manner with a half-maximal inhibitory concentration (IC_{50}) of 20 μg/mL for SeBTT NPs and 25 μg/mL for BBTT NPs, respectively. Furthermore, it can also be noticed that the cell viability remained over 88% when treating HeLa cells with the NPs at a high concentration of 40 μg/mL under dark. These results reveal the predominant photothermal effect, inconsiderable dark cytotoxic effect, and superb biocompatibility of both NPs on HeLa cells. In addition, the cancer ablation performance of SeBTT NPs is superior to that of BBTT NPs. As a result, SeBTT NPs was taken as the representative to execute the subsequent experiments.

In addition, a cell migration assay was performed on HeLa cells further to examine the photothermal therapeutic efficacy of SeBTT NPs (Fig. S9 in Supporting information). The photograph of the cell migration was recorded at different time spots. It is found that HeLa cells were efficiently inhibited from moving in and filling the open gap at 24 h after wounding. This result shows that SeBTT NPs can efficaciously prevent cells from transferring.

As excellent photothermal conversion property *in vitro*, SeBTT NPs were further employed as photoacoustic imaging (PAI) agents to investigate the accumulation tendency of the NPs in living bodies. After systemic administration of SeBTT NPs (150 μg/mL, 100 μL) into xenograft HeLa tumor-bearing nude mice, the photoacoustic images were clearly delineated and quantified at each post-injection time spot. As depicted in Fig. 3, the photoacoustic intensity is very weak at the start of 0 h (pre-scan), which is owing to the NIR absorption from endogenous melanin and hemoglobin. And then, the photoacoustic intensity at tumor sites increased over time and reached the maximum at 6 h post-

injection, and then started to decrease. The real-time *in vivo* photoacoustic intensity extracted from the tumor regions for SeBTT NPs confirmed that the increased photoacoustic signals were generated from SeBTT NPs accumulation, and SeBTT NPs could be real-time monitored over a prolonged period for clinical application. The results of PAI manifest the efficient accumulation of SeBTT NPs in the tumor tissue *via* enhanced permeability and retention (EPR) effect, and also suggest that 6 h post-injection is the optimized time spot for PAI-guided photothermal cancer treatment.

Infrared thermal images were collected as well to monitor the hyperthermia of the tumor site at 6 h post-injection of SeBTT NPs in mice with 808 nm photoirradiation (1.10 W/cm^2). As shown in Fig. S10 (Supporting information), the temperature in the tumor region continually rises along with the irradiation time increasing, and reaches up to 54 °C upon irradiation for 8 min after intravenous tail injection. On the contrary, the group treated with PBS only exhibits little temperature elevation after 8 min light exposure, indicating that photoirradiation alone would have a negligible effect on tumor inhibition. As demonstrate that SeBTT NPs can induce quick temperature increase at tumor sites upon 808-nm photoirradiation, rendering it an efficient nanotheranostic agent for PTT.

To further explore PTT efficacy, SeBTT NPs were next validated with the xenograft HeLa tumor-bearing mouse model. All animal experiments were conducted under the Guide for the Care and Use of Laboratory Animals, approved by the Animal Experimentation Ethics Committee of Nanjing Tech University. The mice that randomly divided into three groups ($n = 5$) were named Group I (PBS + Laser irradiation), Group II (SeBTT NPs only without Laser), and Group III (SeBTT NPs + Laser). Mice in Group I were injected with PBS, while Group II and Group III were treated with SeBTT NPs (150 μg/mL, 100 μL) *via* tail vein injection. The *in vivo* anti-tumor efficacy of all groups through PTT was investigated through examination of the tumor volumes for a period of 16 days. It is presented that the treatment of Group I invalidly suppresses the tumor growth as compared to Group III, suggesting that PBS + Laser irradiation possesses no effect of stopping the tumor from growing. Also, the tumor growth kinetics from Group II is also similar to Group I, which suggests that SeBTT NPs fail to impede the tumor growth in the absence of an 808-nm laser. In other words, only PBS with irradiation or SeBTT NPs itself has negligible active behavior against cancer (Figs. 4a and d). Remarkably, the average tumor volumes of Group III show changes from day 0 that expresses the tremendous anti-tumor efficacy of SeBTT NPs. Then the tumor volumes decrease in the following days (Figs. 4a and c).

After 6-days treatment, the tumors of mice in Group III disappeared, suggesting distinguished cancer cells ablation with 808 nm laser illumination. Meanwhile, the bodyweight of mice in Group III gained gradually (Fig. 4b), indicating the excellent
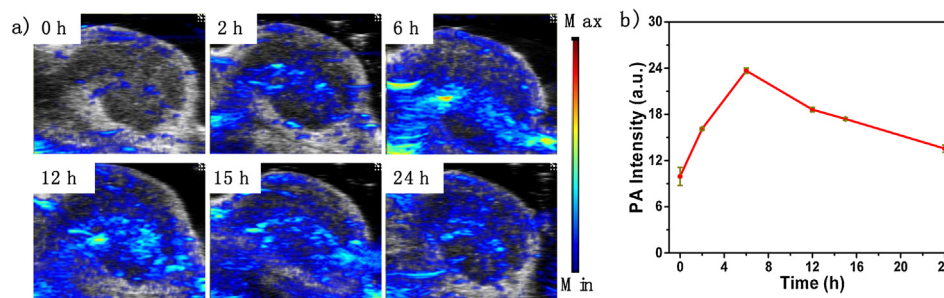

Fig. 3. (a) Photoacoustic imaging of tumor at various times after intravenous tail injection of SeBTT NPs. (b) Photoacoustic intensity in the tumor region against the post-injection time.
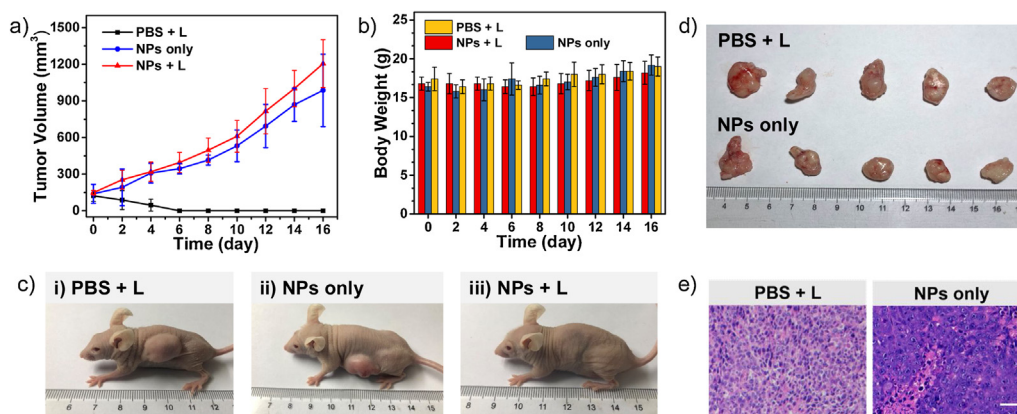
Fig. 4. (a) Tumor growth and (b) bodyweight changes of three groups with different treatments. (c) Photographs of three groups tumor-bearing mice after treatment. (d) The mice tumors collected with Group I and Group II. (e) H&E stained images of the tumor tissues after treatment. Scale bar: 100 μm.

biosafety and low side toxic effect of SeBTT NPs. All the results demonstrate that SeBTT NPs can serve as an excellent nano-agent for PTT. After 16-days treatment *in vivo*, the mice in all groups were executed, and the tissues of tumor and main organs were collected for histopathological examination using hematoxylin and eosin (H&E) staining to comprehend the therapeutic efficacy at cellular level. Fig. 4e records the photographs of the tumor histologic section of Group I and Group II. It is found that the tumor cells are arranged closely, and the nuclei of tumor cells are in good order. Moreover, the H&E staining of main organs from different treatment groups illustrates that there is no noticeable damage of histological morphology of the groups with SeBTT NPs injection, comparing to the PBS injection group (Fig. S11 in Supporting information). The photography of the organs shows that the cells' nuclear remains almost unchanged. All results indicate that SeBTT NPs are equipped with a high bio-compatibility without any noticeable side effects to living mice *in vivo*.

In summary, two near-infrared absorbing organic small molecular dyes SeBTT and BBTT were developed through D-A-D structural design, and showed intensive NIR absorbance and high molar extinction coefficient. Hydrophilic SeBTT NPs and BBTT NPs were obtained after nano-precipitation and showing remarkable photothermal conversion efficacy of 65.3% and 55.1%, respectively. *In vitro* experiments illustrate that both SeBTT NPs and BBTT NPs can effectively kill the HeLa cells in a dose-dependent manner with low half-maximal inhibitory concentration (IC_{50}) of 20 μg/mL and 25 μg/mL, respectively. With a xenograft HeLa tumor-bearing nude mouse model, photoacoustic imaging-guided photothermal therapy is studied for SeBTT NPs, which illustrate that SeBTT NPs can efficiently kill the tumors in living mice without noticeable side effect to main organs. It is suggested that molecular surgery strategy through heteroatom substitution is effective to regulate the photothermal properties of NIR small molecules for enhanced photoacoustic imaging and photothermal therapy.

Declaration of competing interest

The authors declare that they have no known competing financial interests or personal relationships that could have appeared to influence the work reported in this paper.

Acknowledgments

Appendix A. Supplementary data

Supplementary material related to this article can be found, in the online version, at doi:https://doi.org/10.1016/j.cclet.2021.02.017.

References

[1] H.S. Jung, P. Verwilst, A. Sharma, et al., Chem. Soc. Rev. 47 (2018) 2280–2297.
[2] G. Feng, G.Q. Zhang, D. Ding, Chem. Soc. Rev. 49 (2020) 8179–8234.
[3] D. Chen, Z. Zhong, Q. Ma, et al., ACS Appl. Mater. Interfaces 12 (2020) 26914–26925.
[4] W. Hu, X. Miao, H. Tao, et al., ACS Nano 13 (2019) 12006–12014.
[5] M. Chen, X. Zhang, J. Liu, et al., ACS Nano 14 (2020) 4265–4275.
[6] Y. Cai, W. Si, W. Huang, et al., Small 14 (2018) 1704247.
[7] Y. Xiao, F. An, J. Chen, et al., Small 15 (2019) 1903121.
[8] Q. Xia, Z. Chen, Z. Yu, et al., ACS Appl. Mater. Interfaces 10 (2018) 17081–17088.
[9] J. Weber, P.C. Beard, S.E. Bohndiek, Nat. Methods 13 (2016) 639–650.
[10] A. de la Zerda, S. Bodapati, R. Teed, et al., ACS Nano 6 (2012) 4694–4701.
[11] J. Li, K. Pu, Chem. Soc. Rev. 48 (2019) 38–71.
[12] Y. Jiang, P.K. Upputuri, C. Xie, et al., Adv. Mater. 31 (2019) 1808166.
[13] D. Cui, P. Li, X. Zhen, et al., Adv. Funct. Mater. 29 (2019) 1903461.
[14] Z. Wang, P.K. Upputuri, X. Zhen, et al., Nano Res. 12 (2019) 49–55.
[15] Y. Chen, L. Li, W. Chen, H. Chen, J. Yin, Chin. Chem. Lett. 30 (2019) 1353–1360.
[16] W. Hu, P.N. Prasad, W. Huang, Acc. Chem. Res. 54 (2020) 697–706.
[17] X. Yang, G. Liu, Y. Shi, et al., Nanotechnology 29 (2018) 222001.
[18] L. Cheng, C. Wang, L. Feng, K. Yang, Z. Liu, Chem. Rev. 114 (2014) 10869–10939.
[19] Y. Yang, Y. Yu, H. Chen, et al., ACS Nano 14 (2020) 13536–13547.
[20] P. Liang, Q. Tang, Y. Cai, et al., Chem. Sci. 8 (2017) 7457–7463.
[21] X. Gu, X. Zhang, H. Ma, et al., Adv. Mater. 30 (2018) 1801065.
[22] J. Qi, C. Chen, X. Zhang, et al., Nat. Commun. 9 (2018) 1848.
[23] N. Shi, Y. Shi, J. Shao, et al., Dyes Pigm. 160 (2019) 683–691.
[24] H.S. Jung, J.H. Lee, K. Kim, et al., J. Am. Chem. Soc. 139 (2017) 9972–9978.
[25] H.S. Jung, J. Han, J.H. Lee, et al., J. Am. Chem. Soc. 137 (2015) 3017–3023.
[26] S. Luo, X. Tan, S. Fang, et al., Adv. Funct. Mater. 26 (2016) 2826–2835.
[27] X. Tan, S. Luo, L. Long, et al., Adv. Mater. 29 (2017) 1704196.
[28] C. Wu, X. Huang, Y. Tang, et al., Chem. Commun. 55 (2019) 790–793.
[29] P. Liang, Q. Tang, Y. Cai, et al., Chem. Sci. 8 (2017) 7457–7463.
[30] Y. Jiang, J. Li, X. Zhen, C. Xie, K. Pu, Adv. Mater. 30 (2018) 1705980.
[31] C. Yang, X. Wang, S. Huang, M. Wang, Adv. Funct. Mater. 28 (2018) 1705226.
[32] L. Shi, F. Hu, Y. Duan, et al., ACS Nano 14 (2020) 2183–2190.
[33] D. Chen, Q. Tang, J. Zou, et al., Adv. Healthc. Mater. 7 (2018) 1701272.
[34] Y. Tang, L. Xue, Q. Yu, et al., ACS Appl. Bio Mater. 2 (2019) 5888–5897.
[35] Q. Tang, W. Xiao, C. Huang, et al., Chem. Mater. 29 (2017) 5216–5224.
[36] W. Lin, D. Colombani-Garay, L. Huang, C. Duan, G. Han, WIREs Nanomed. Nanobiotechnol. 12 (2020) 1–15.
[37] S. Li, Q. Deng, Y. Zhang, et al., Adv. Mater. 32 (2020) 2001146.
[38] J. Li, D. Cui, J. Huang, et al., Angew. Chem. 58 (2019) 12680–12687.
[39] D. Chen, Q. Yu, X. Huang, et al., Small 16 (2020) 2001059.
[40] D. Chen, Z. Wang, H. Dai, et al., Small Methods 4 (2020) 2000013.
[41] Z. Zhang, W. Xu, M. Kang, et al., Adv. Mater. 32 (2020) 2003210.
[42] K. Wang, W. Ma, Y. Xu, et al., Chin. Chem. Lett. 31 (2020) 3149–3152.
[43] R. Boyd, Nat. Chem. 3 (2011) 570.
[44] G. Mugesh, H.B. Singh, Chem. Soc. Rev. 29 (2000) 347–357.
[45] Q. Wu, Y. Yuan, F. Chen, et al., ACS Macro Lett. 9 (2020) 1547–1551.
[46] C. Sun, Y. Tan, H. Xu, ACS Mater. Lett. 2 (2020) 1173–1177.
[47] J. Yang, S. Pan, S. Gao, Y. Dai, H. Xu, Biomaterials 249 (2020) 120054.

[48] K. Ono, S. Tanaka, Y. Yamashita, Angew. Chem. 33 (1994) 1977–1979.
[49] F. Ye, W. Chen, Y. Pan, S.H. Liu, J. Yin, Dyes Pigm. 171 (2019) 107746.
[50] H. Li, H. Wen, Z. Zhang, et al., Angew. Chem. 59 (2020) 20371–20375.
[51] T. Dong, K. Wen, J. Chen, et al., Adv. Funct. Mater. 28 (2018) 1800135.
[52] Y. Wang, T. Hasegawa, H. Matsumoto, T. Mori, T. Michinobu, Adv. Funct. Mater. 27 (2017) 1604608.
[53] T.L.D. Tam, W. Ye, H.H.R. Tan, et al., J. Org. Chem. 77 (2012) 10035–10041.
[54] Y. Wang, T. Hasegawa, H. Matsumoto, T. Mori, T. Michinobu, Adv. Mater. 30 (2018) 1707164.
[55] G. Qian, B. Dai, M. Luo, et al., Chem. Mater. 20 (2008) 6208–6216.
[56] L. Tu, Y. Xu, Q. Ouyang, X. Li, Y. Sun, Chin. Chem. Lett. 30 (2019) 1731–1737.
[57] H. Zhou, Y. Xiao, X. Hong, Chin. Chem. Lett. 29 (2018) 1425–1428.
[58] J. Shao, J. Chang, C. Chi, Org. Biomol. Chem. 10 (2012) 7045–7052.
[59] J. Shao, X. Guo, N. Shi, et al., Sci China Mater. 62 (2019) 497–507.
[60] T.L. Tam, H. Li, Y.M. Lam, S.G. Mhaisalkar, A.C. Grimsdale, Org. Lett. 13 (2011) 4612–4615.
[61] J. Shao, G. Wang, K. Wang, C. Yang, M. Wang, Polym. Chem. 6 (2015) 6836–6844.
[62] J. Shao, Z. Guan, Y. Yan, et al., J. Org. Chem. 76 (2011) 780–790.
[63] S. Sasaki, G.P.C. Drummen, G. Konishi, J. Mater. Chem. C 4 (2016) 2731–2743.
[64] X. Yang, Q. Yu, N. Yang, et al., J. Mater. Chem. B 7 (2019) 2454–2462.
[65] D. Chen, J. Zhang, Y. Tang, et al., J. Mater. Chem. B 6 (2018) 4522–4530.
[66] D. Xi, M. Xiao, J. Cao, et al., Adv. Mater. 32 (2020) 1907855.